Chapter 5

Influence of NaCl Environment on Elastic-Plastic Fracture behavior of Al-Mg-Zn Alloy

5.1 Introduction

We investigated the elastic plastic J1c fracture toughness of Solution heat treated (SHT), SHT+ peak aged (PA), SHT+45% cold rolled (CR), SHT+60% warm rolled (WR) and SHT+PA+90% CR Al-Mg-Zn alloy in 3.5% NaCl solution. An electrochemical workstation (Gamry Interface 1010 E) was used for electrochemical testing. Transmission electron microscopy (TEM) and scanning electron microscopy (SEM) are used to study microstructure. Tensile testing, Vickers hardness testing, and the elastic plastic J1c fracture toughness test is used to examine mechanical properties. Because of the lack of precipitates and passivation through dislocations, the SHT+45% CR sample had the lowest Ecorr (0.4 V) and Icorr (8.16 µA) and the highest corrosion resistance (highest polarisation resistance with highest corrosion life; 9.869e-08 mmpy); however, its mechanical properties were inferior. In contrast, the SHT + PA + 90% CR sample was found to be optimal, offering a good balance of mechanical strength (hardness (226 HV in normal condition, 180±5 in 3.5% NaCl solution), maximum tensile strength (526±5 MPa in normal condition,400±5 MPa in 3.5% NaCl solution) and maximum conditional fracture toughness JQ (344.54±10 kJ/m2 in normal condition, 225±7 kJ/m2 in 3.5% NaCl condition) and improved corrosion resistance (corrosion life 5.827e-5 mmpy, Ecorr (0.58 V) and Icorr (10.15 µA)) although slightly lower than the SHT+45% CR and SHT conditions but better than SHT+PA and SHT+60% WR sample, owing to the formation of redistributed, very fine precipitates, large no. of sub grains and enhanced passivation via high dislocation density. SHT+PA

sample has lowest corrosion resistance due to having large number of precipitates which are acting as galvanic sites to increase corrosion rate (lowest polarization resistance with lowest corrosion life (2.904e-01mmpy) and lowest Ecorr (0.7 V) and Icorr (26.27 μA)).

5.2 Microstructural investigation

5.2.1 SEM

Fig. 5.1(a) is SEM image of SHT sample in normal condition and Fig. 5.1(b) is SEM image of SHT+PA sample in normal condition, Fig. 5.1(c), (d) and (e) are the SEM image of SHT+45% CR, SHT+60% WR and SHT+PA+90% CR sample respectively in normal condition.

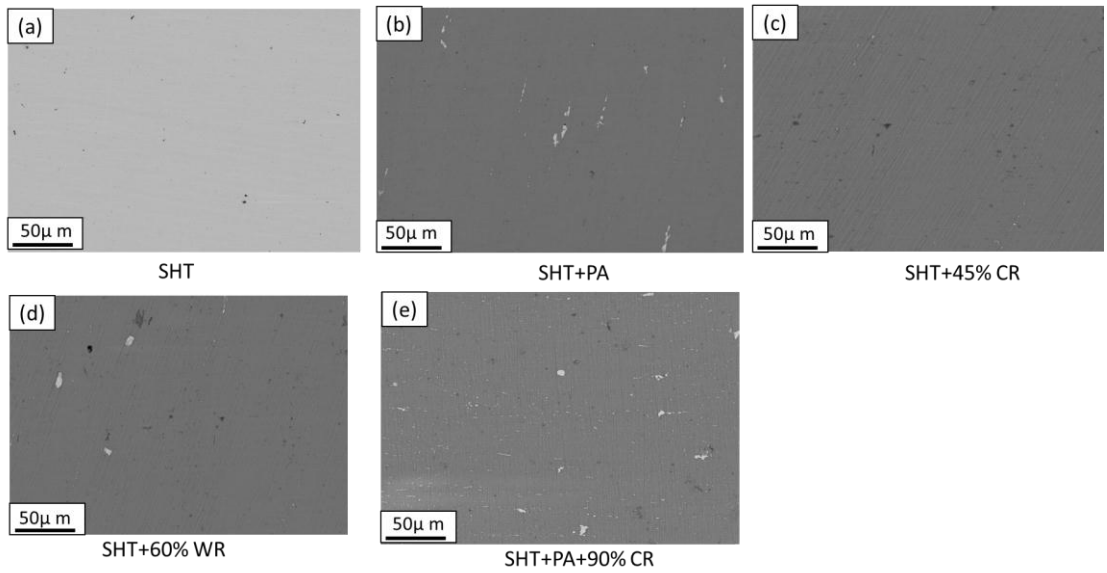

Fig.5.1 FE SEM image of SHT, SHT+PA, SHT+45% CR, SHT+60% WR, and SHT+PA+90% CR samples in normal condition]

Fig. 5.2(a) is SEM image of SHT sample in 3.5% NaCl solution in which less no. of pits but of larger size is observed while in Fig. 5.2(b) which is the SEM image of SHT+PA sample, larger number of pits with large size is observed. Fig. 5.2(c) is SEM

image of SHT+45% CR sample wherein very small no. of pits with very small size is noticed whereas in SHT+60% WR sample (Fig.5.2(d)) large size of pits in large no. (less than SHT+PA sample) is spotted. Fig. 5.2(e) is SEM image of SHT+PA+90% CR sample in which very small size pit (same as SHT+45% CR sample) but in moderate no. (more than SHt+45% CR sample but less than SHT+PA and SHT+60% WR sample)

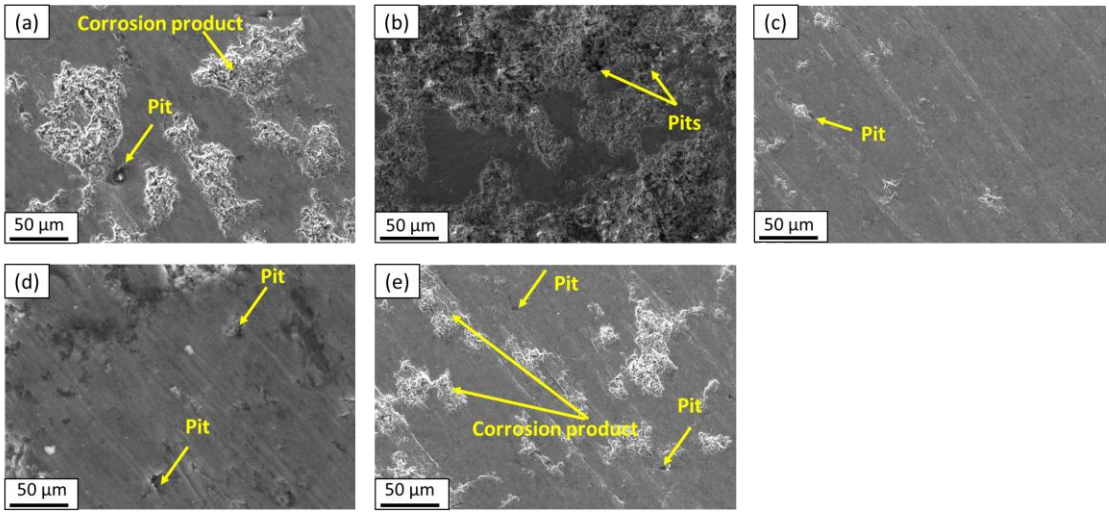

Fig.5.2 SEM images of SHT, SHT+PA, SHT+45% CR, SHT+60% WR, and SHT+PA+90% CR in 3.5% NaCl solution

5.2.2 TEM

From the TEM image it is clear that no precipitate (only dispersoids) in SHT sample (Fig.5.3(a), (b)) whereas maximum precipitation with grain boundary precipitation is observed in SHT+PA sample (Fig 5.4(a), (b), (c)), while coarse precipitation is observed in SHT+60% WR sample (Fig. 5.5(c), (d) (e)). SHT+45% CR sample TEM image showing larger sub-grains formation in small no. (Fig. 5.6(a), (b)) while in SHT+PA+90% CR sample is showing very small size of sub-grains in large no. (5.7(a), (b)) with redistributed very fine precipitates (Fig. 5.7 (c), (d) (e)).

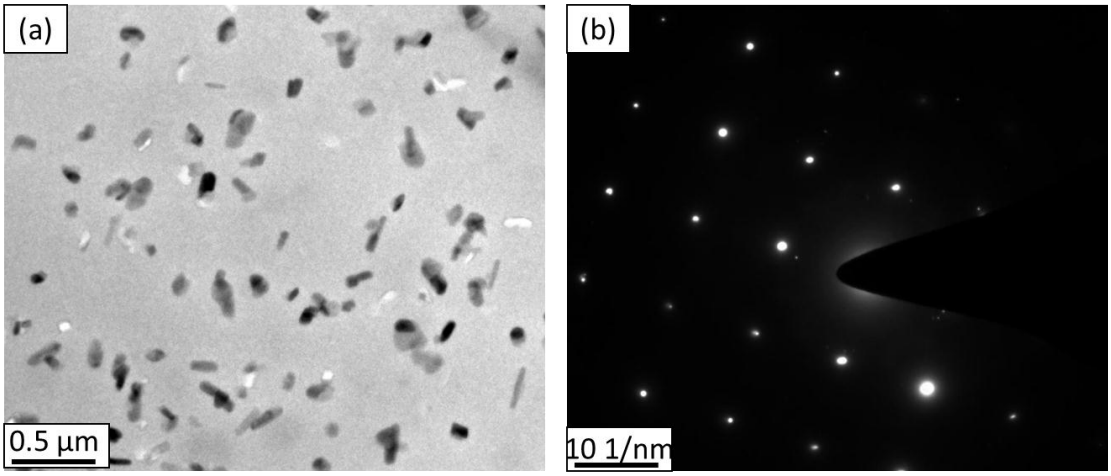

Fig.5.3 (a) Bright field image of SHT sample, (b) SAED pattern of SHT sample

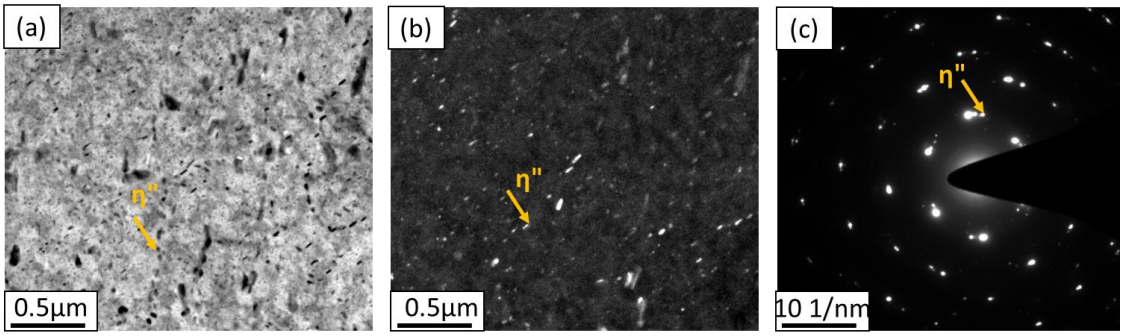

Fig.5.4 (a) Bright field image of SHT+PA sample, (b) dark field image of SHT+PA sample, (c) SAED pattern of SHT+PA sample

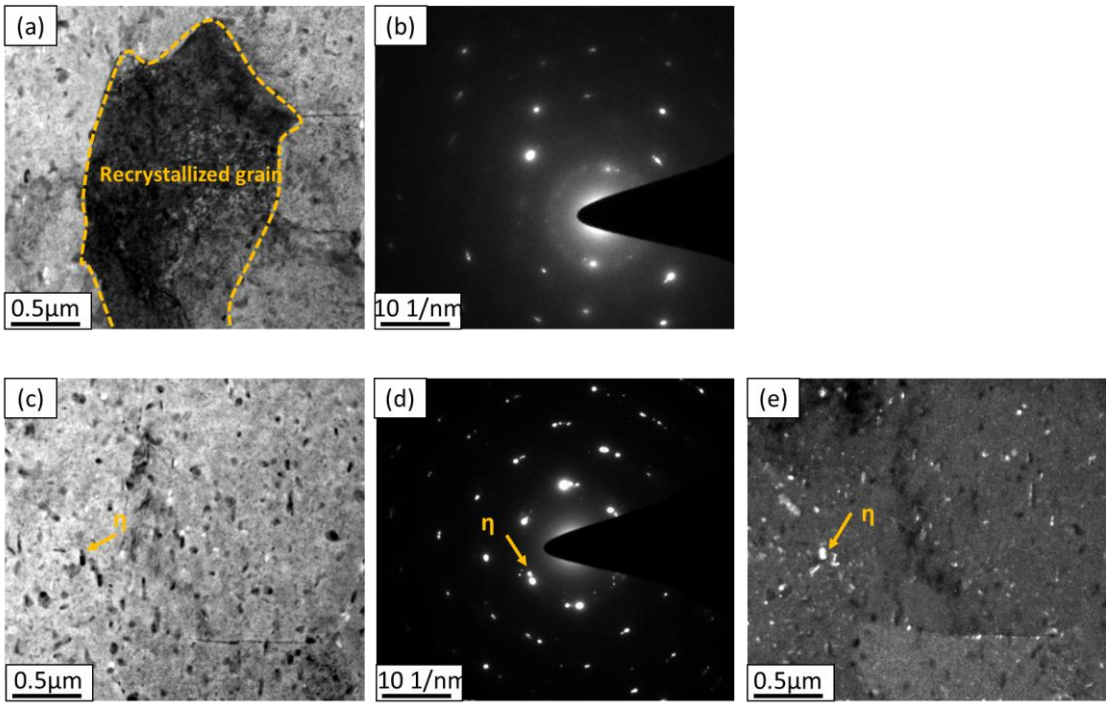

Fig.5.5 (a) Bright field image of SHT +60% WR sample, (b) SAED pattern of SHT+60% WR sample, (c) Bright field image of SHT +60% WR sample, (d) SAED pattern of SHT+60% WR sample, (e) dark field image of SHT+60% WR sample

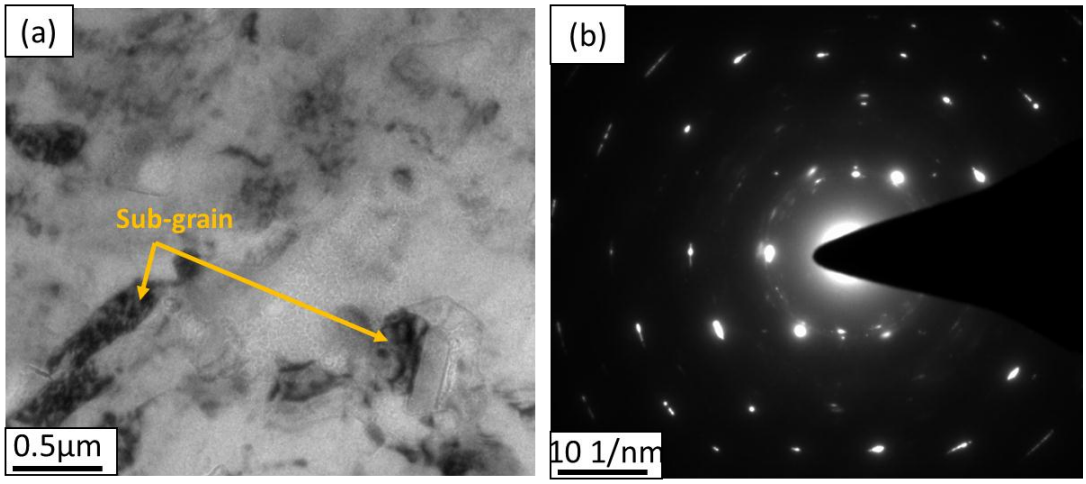

Fig.5.6 (a)Bright field image of SHT +45% CR sample, (b) SAED pattern of SHT+45% CR sample

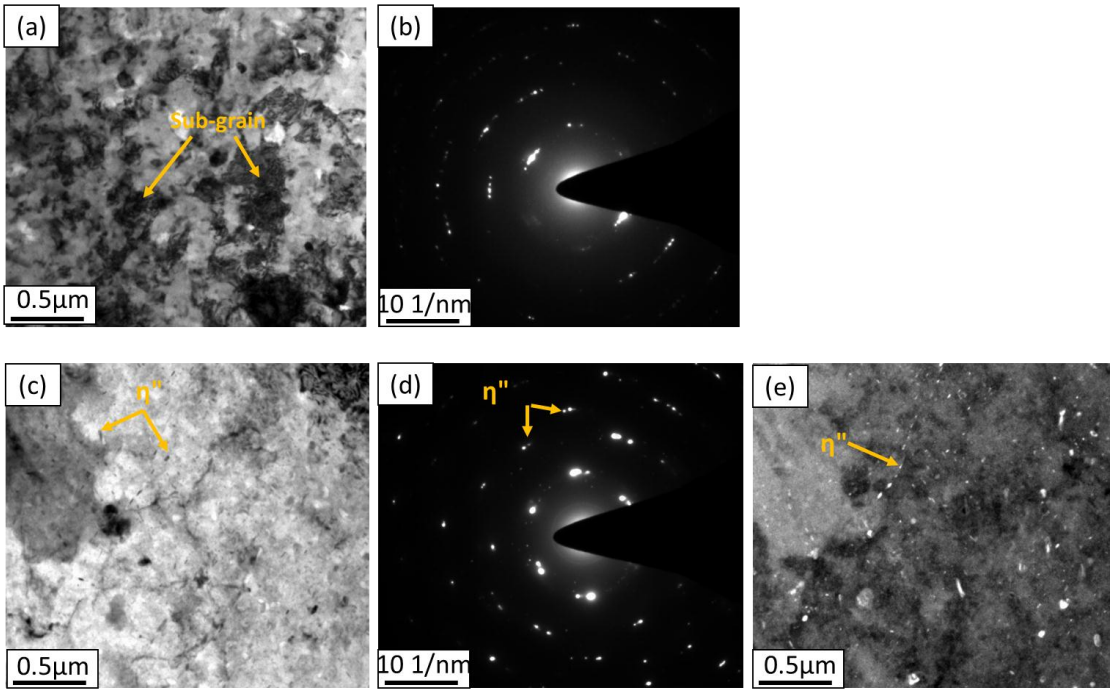

Fig.5.7 (a) Bright field image of SHT+PA+90% CR sample, (b) SAED pattern of SHT+PA+90% CR sample, (c) Bright field image of SHT+PA+90% CR sample, (d) SAED pattern of SHT+PA+90% CR sample, (e) dark field image of SHT+PA+90% CR sample

5.3 Corrosion testing

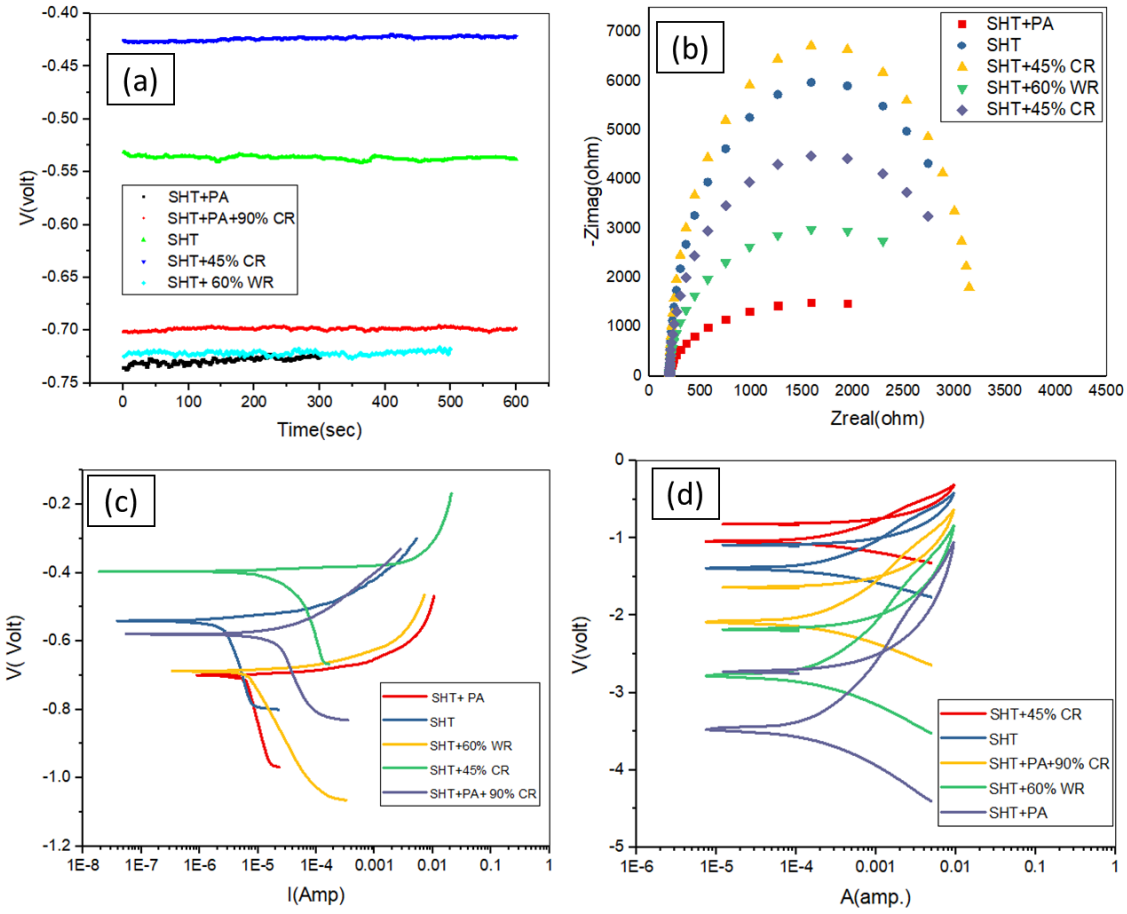

Fig.5.8 (a) OCP plot, (b) Nyquist plot, (c) Tafel plot, (d) Cyclic polarization plot of SHT, SHT+PA, SHT+45% CR, SHT+60% WR, and SHT+PA+90% CR

5.3.1 Open circuit potential (OCP) test

Fig.5.8 (a) is showing the OCP plot for all five conditions samples. Corrosion potential value for SHT+45%, SHT+PA, SHTCR, SHT+60% WR, and SHT+PA+90% CR are -0.43, -0.74, -0.53, -0.73 and -0.7

5.3.2 Nyquist plot

Fig. 5.8 (b) is showing Nyquist plot for all five conditions samples (SHT, SHT+PA, SHT+45% CR, SHT+60% WR, and SHT+PA+90% CR). From Fig. 12(b) it is clear that diameter of SHT45% CR sample is higher as compared to all other samples.

Decreasing order of diameter in Fig. 12(b) is described as SHT+45%CR >SHT> SHT+PA+90% CR > SHT+60% WR > SHT+PA

5.3.3 Tafel plot

Fig.5.8 (c) is showing the Tafel plot for all five conditions samples (SHT, SHT+PA, SHT+45% CR, SHT+60% WR, and SHT+PA+90% CR). Ecorr., Icorr. And corrosion rate values for all five conditions are described in Table 5.1.

Table 5.1. Ecorr., Icorr. and corrosion rate values for all five conditions samples

Samples	**Ecorr (Volt)**	**Icorr (μA)**	**Corrosion rate(mmpy)**
SHT+ 45% CR	0.4	8.16	9.869e-08
SHT+PA	0.7	26.27	2.904e-01
SHT	0.51	9.67	9.413e-6
SHT+ 60% WR	0.68	15.39	1.546e-3
SHT+PA+90% CR	0.58	10.15	5.827e-5

5.3.4 Cyclic polarization curve

Fig. 5.8 (d) is showing cyclic polarization plot for all five conditions samples of SHT, SHT+PA, SHT+45% CR, SHT+60% WR, and SHT+PA+90% CR. From Fig. 5.8 (d) it is clear that loop of SHT+45% CR sample has smaller as compared to all other four samples.

5.4 Mechanical testing

5.4.1 Hardness testing

Fig. 5.9 is showing hardness graph of all five conditions samples (SHT, SHT+PA, SHT+45% CR, SHT+60% WR, and SHT+PA+90% CR) in 3.5% NaCl solution and normal condition

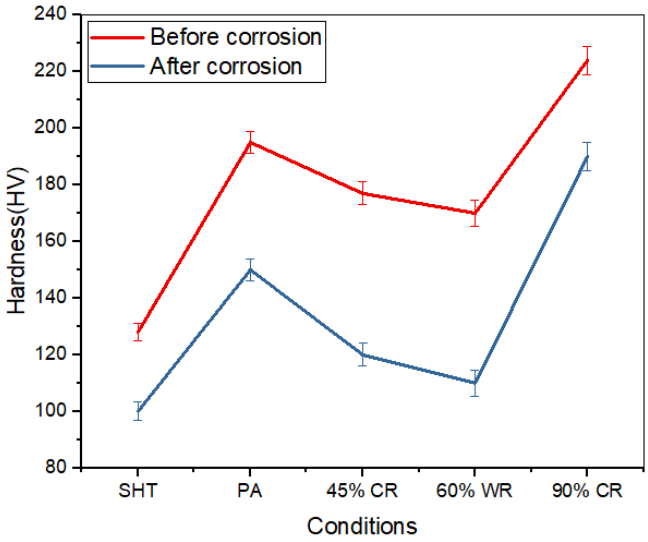

Fig.5.9 Hardness graph of all five samples (SHT, SHT+PA, SHT+45% CR, SHT+60% WR, and SHT+PA+90% CR) in 3.5% NaCl and solution and normal condition

5.4.2 Tensile testing

Fig.5.10 is showing the tensile test graph for all five conditions samples (SHT, SHT+PA, SHT+45% CR, SHT+60% WR, and SHT+PA+90% CR) in 3.5 % NaCl solution and Normal condition. The value of yield point, Ultimate tensile strength (UTS) and % elongation for all five conditions samples in is described in Table 5.2

Table 5.2. The value of yield point, Ultimate tensile strength (UTS) and % elongation for all five conditions samples in 3.5 % NaCl solution

Condition	**Yield point (MPa)**	**UTS(MPa)**	**%elongation**
As received	300.8±4	350.8±4	9±2%
SHT	100±8	150±5	10±1%
SHT+PA	350±9	400.5±8	7±2%
SHT+ 45% CR	200±10	250± 6	8±1%,
SHT+ 60% WR	170±7	200± 7	10±3%
SHT+PA+90% CR	370±10	400±4	6±2%

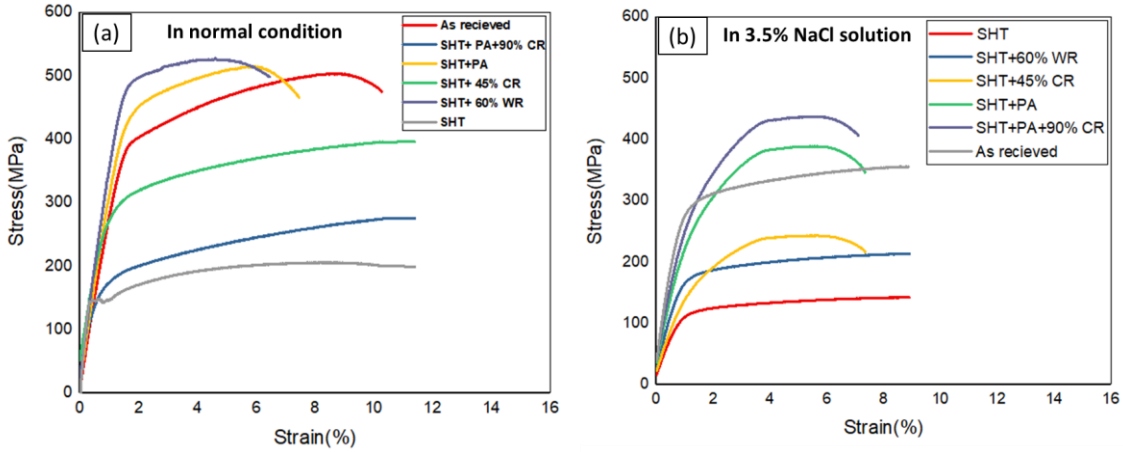

Fig.5.10 Tensile test graph of all five samples (SHT, SHT+PA, SHT+45% CR, SHT+60% WR, and SHT+PA+90% CR) in (a) normal condition. (b) 3.5% NaCl and solution condition

5.4.3 Elastic plastic J_{1c} fracture test

The load point displacement method, as previously described in chapter 3 in section 3.3.3, was employed to evaluate the conditional fracture toughness (J_Q) of samples under five different conditions. To validate the determination of elastic-plastic fracture toughness, the minimum required values for unbroken ligament length (b) and sample thickness (B) were identified as 17.394 mm for the SHT+PA+90% CR condition, 16.34 mm for SHT+PA, and 13.5 mm for SHT, 15.12 mm for SHT+45% CR and 14.58 mm for SHT+60% WR conditions [[148]]. In the present study, b and B were similarly calculated for the all five condition samples after corrosion in 3.5% NaCl solution, yielding B values of 7.12 mm ,10.51 mm, 9.76mm, 8.34 and 12.98 for SHT, SHT+PA, SHT+45% CR, SHT+60% WR, and SHT+PA+90% CR respectively. However, the actual sample thickness used was 5.7 mm, and the unbroken ligament length was 25.4 mm. As a result, the calculated B values for all conditions PA, SHT, SHT+45% CR, SHT+60% WR, and SHT+PA+90% CR did not meet the criteria specified by Eq. (3.6) in chapter 3. Given that the required thickness conditions were unmet and preparing

thicker specimens was impractical, the fracture toughness values obtained represent conditional fracture toughness (J_Q) rather than true J_1 c values. Table 5.3 summarizes the conditional fracture toughness for each condition, and Fig.5.11 presents the load point displacement curves corresponding to all five conditions.

Table 5.3. The value of conditional fracture toughness (J_Q) for all five conditions samples in normal condition and 3.5 % NaCl solution condition

Samples	Conditional fracture toughness (J_Q) (kJ/m2) in normal condition	Conditional fracture toughness (J_Q) (kJ/m2) in NaCl condition
SHT	82.5±5	70±4
SHT+PA	230.35±7	190±5
SHT+45% CR	180± 5	170±5
SHT+60% WR	150± 5	130±4
SHT+PA+90% CR	344.54±10	225±7

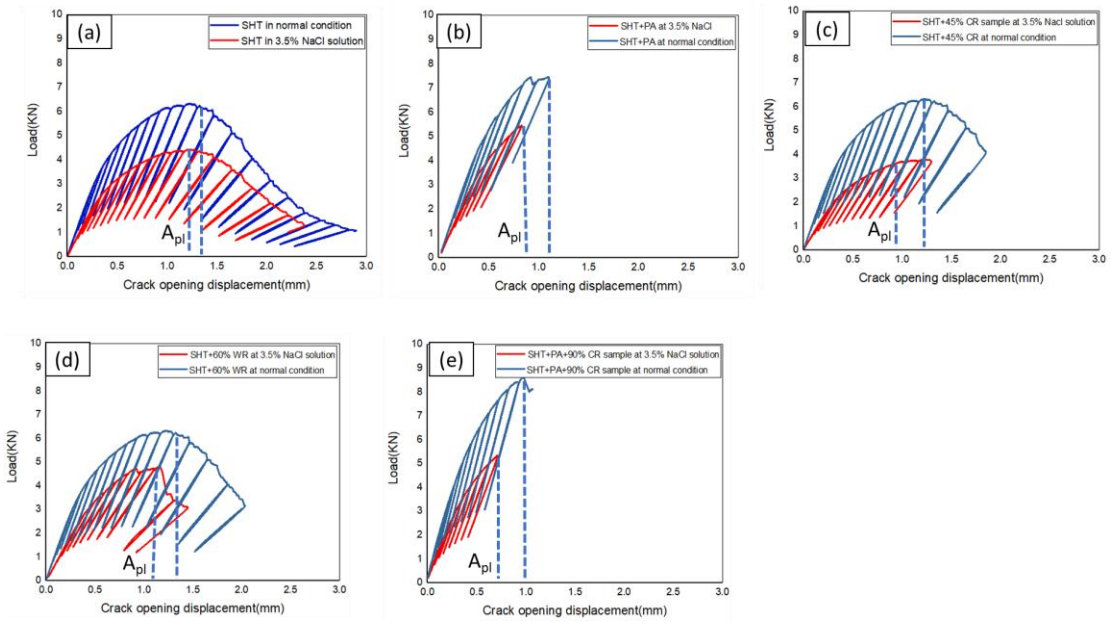

Fig.5.11 Load vs crack opening displacement Conditional five samples (SHT, SHT+PA, SHT+45% CR, SHT+60% WR, and SHT+PA+90% CR) in 3.5% NaCl solution and normal condition

5.5 Fractography

Fig. 5.12 and Fig. 5.13 are illustrating the fractography image of the fractured tensile sample of all five conditions (SHT, SHT+PA, SHT+45% CR, SHT+60% WR, and SHT+PA+90% CR) in normal and in 3.5% NaCl condition respectively. The large ductile dimples are observed in SHT sample in normal condition (Fig.5.12(a)) while in 3.5% NaCl solution smaller dimples with some facets are observed showing brittle fracture (Fig. 5.13(a)). Similarly, in SHT+PA (Fig.5.13(b)), SHT+45% CR, SHT+60% WR and SHT+PA+90% CR samples brittle fracture is dominated in 3.5% NaCl solution with smaller dimple and large facets along with some corrosion product on fractured surface.

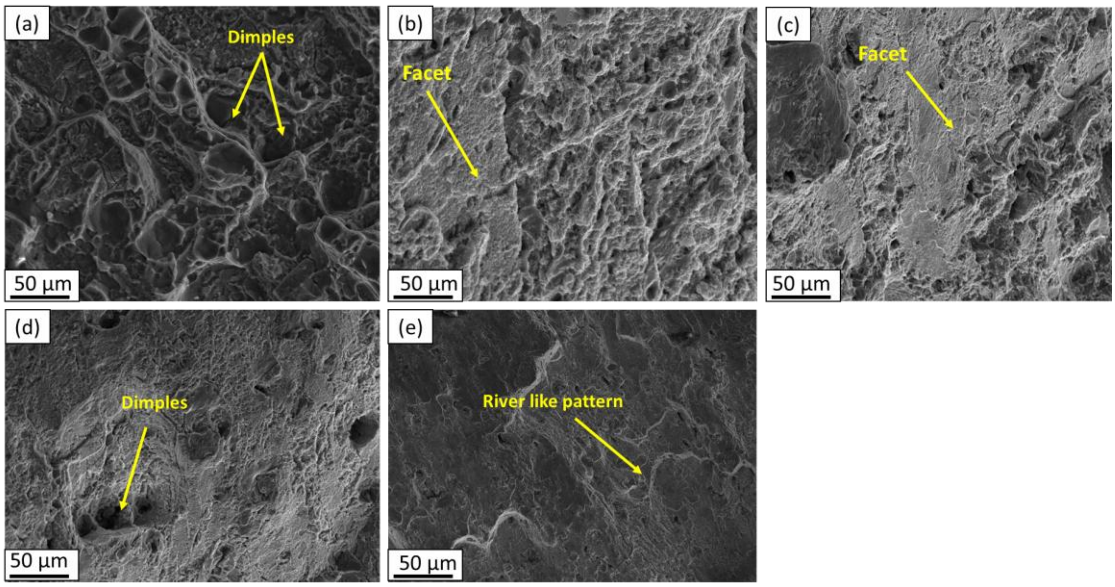

Fig. 5.12 Fractography image of fractured tensile sample of (a) SHT sample in normal condition, (b) SHT+PA sample in normal condition, (c) SHT+ 45% CR sample in normal condition, (d) SHT+60% WR sample in normal condition, (e) SHT+PA+90% CR sample in normal condition

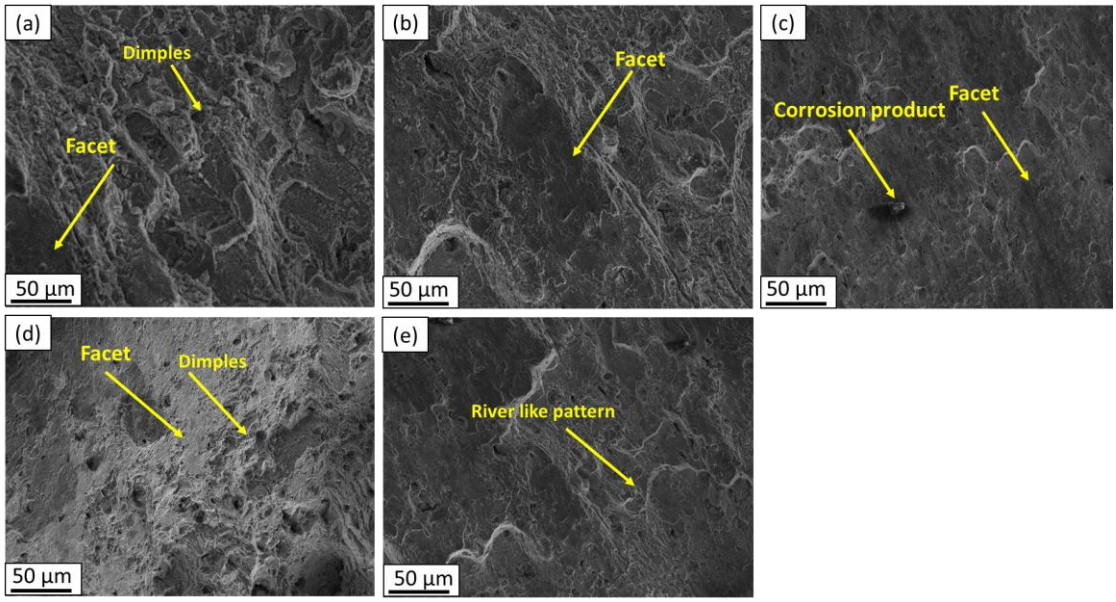

Fig. 5.13 Fractography image of fractured tensile sample of (a) SHT sample in 3.5% NaCl solution condition (b) SHT+PA sample in 3.5% NaCl solution condition (c) SHT+ 45% CR sample in 3.5% NaCl solution condition (d) SHT+60% WR sample in 3.5% NaCl solution condition (e) SHT+PA+90% CR sample in 3.5% NaCl solution condition

Fig. 5.14 and Fig. 5.15 are demonstrating the fractography image of J_{1c} fractured CT sample for all five conditions samples (SHT, SHT+PA, SHT+45% CR, SHT+60% WR, and SHT+PA+90% CR) in normal and 3.5% NaCl condition. Which is supporting the tensile test result that is brittle fracture is preferred in 3.5% NaCl solution with small ductile dimples and smooth and shiny facets with corrosion products.

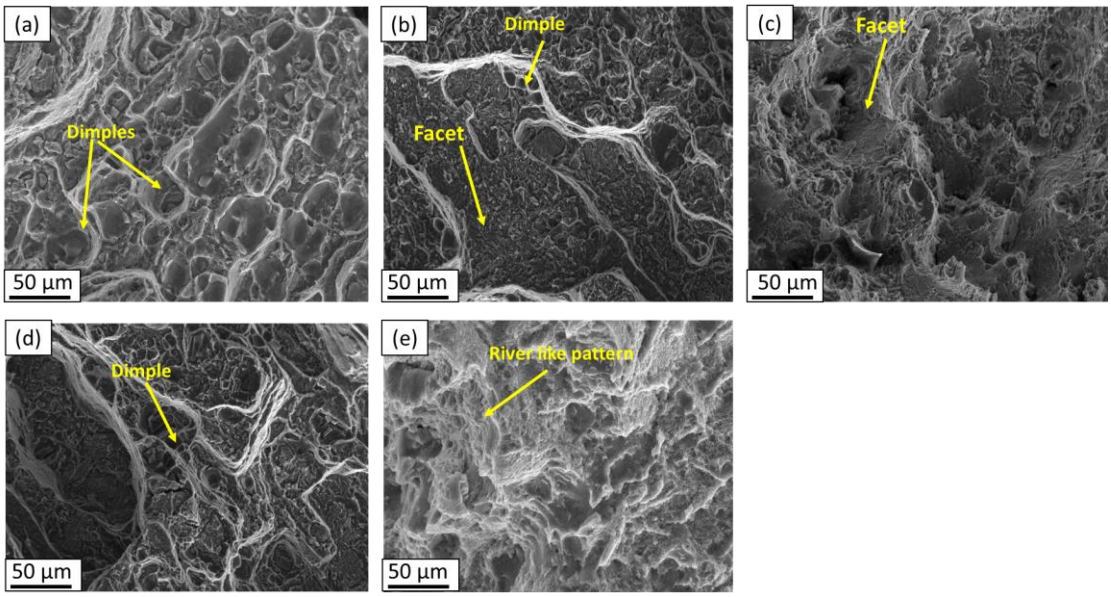

Fig. 5.14 Fractography image of CT sample of (a) SHT sample in normal condition, (b) SHT+PA sample in normal condition, (c) SHT+ 60% WR sample in normal condition, (d) SHT+45% CR sample in normal condition, (e) SHT+PA+90% CR sample in normal condition

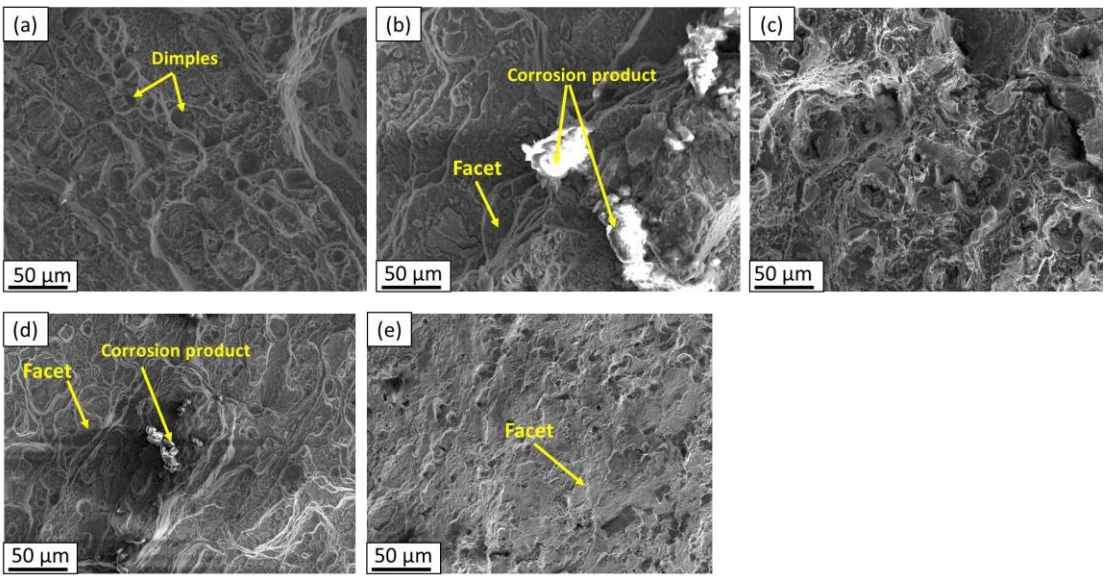

Fig. 5.15 Fractography image of CT sample of (a) SHT sample in 3.5% NaCl solution condition (b) SHT+PA sample in 3.5% NaCl solution condition (c) SHT+ 60% WR sample in 3.5% NaCl solution condition (d) SHT+45% CR sample in 3.5% NaCl solution condition (e) SHT+PA+90% CR sample in 3.5% NaCl solution condition

5.6. Discussion

5.6.1 Microstructural correlation with corrosion behaviour

The SHT sample exhibits a small number of large-sized pits (Fig. 5.2(a)). This is because, in SHT condition super saturated solid solution is formed and there are no precipitates in matrix as well as on grain boundary (Fig.5.3(a)), but once corrosion initiates, there are no barriers in the SHT condition to hinder its progression[81]. Therefore, pit size is large. SHT+PA sample exhibits a greater number and larger size of corrosion pits (Fig. 5.2(b)) compared to the, SHT+45% CR (Fig. 6(c)), SHT+60% WR (Fig. 5.2(d)), and SHT+PA+90% CR (Fig. 5.2(e)) samples. This is attributed to the higher density of precipitates present both within the matrix and along grain boundaries (Fig. 5.4(a)), which act as galvanic sites, initiating the corrosion process[106,149]. The SHT+60% WR sample, processed at 200°C, contains coarse precipitates (Fig. 5.5(a)) due to warm rolling[38,131] In contrast, the SHT+45% CR samples show an absence of precipitates (Fig. 5.6(a)). Additionally, the SHT+45% CR sample exhibits a limited formation of sub-grains and dislocations (Fig. 5.6(a)), resulting in the highest corrosion resistance for the SHT+45% CR sample[79]. In the SHT+PA+90% CR sample, the high distortion energy from severe deformation helps dissolve most precipitates[108], with the remaining fine precipitates redistributed within the matrix (Fig. 5.7(c)). This intense deformation also leads to the formation of numerous sub-grains and dislocations (Fig. 5.7(a)), which enhance passivation[150] and provide optimal corrosion resistance[106,128]. OCP of SHT+45% CR sample is noble (Fig.5.8(a)) than all other samples and having more polarization resistance (Fig.5.8 (b)) along with lower Icorr, Ecorr and better corrosion life (Fig. 5.8(c), Table 5.1) as well as less chances of pitting corrosion (Fig. 5.8 (d)) because having no precipitates on grain boundary and matrix

and passivation through dislocation and sub grain formation. But it is reverse in case of SHT+PA sample because Peak aging forms fine, dense precipitates (η" Mg_2Zn_3)[124], which is creating electrochemical potential differences. Grain boundary precipitation leads to localized attack, especially pitting corrosion[39]. Fractography image of all five conditions sample (Fig. 5.13, Fig. 5.15) is showing brittle fracture is dominated in 3.5% NaCl solution due to formation of corrosion pits plastic deformation is reduced[151] and brittle fracture is preferred with small dimples and large shiny, bright facets[97,98]. The corrosion product is also visible on the fractured surface, indicating that all samples have experienced corrosion not only on the exterior but also internally[15,152].

5.6.2 Mechanical property in 3.5% NaCl solution

Strength and hardness of SHT+PA+90% CR sample is highest (figs.5.9, 5.10 (a, b)) due to the formation of large number of sub-grains (Fig. 11(a)) and higher dislocation density along with grain boundary strengthening[124].Strength and hardness of SHT+PA sample is higher(figs. 5.9, 5.10 (a, b))) due to precipitation hardening(Fig.5.4(a)) and it is lowest in SHT (figs. 5.9, 5.10 (a, b))) because there is no precipitate(Fig.7(a)) in this case[31,130]. Strength and hardness of SHT+ 45% CR sample is more as compared to SHT+60% WR sample (figs. 5.9, 5.10 (a, b))) because in SHT+45% CR sample due to light deformation small number of sub-grains and dislocations (Fig. 5.6(a)) has formed which creating obstruction in movement of dislocation. While in SHT+60% WR sample recrystallized grains (Fig. 5.5(a)) are formed with coarse precipitation of (Fig. 5.5(c)). Strength and hardness of all five conditions sample is decreasing in 3.5% NaCl solution because corrosion reactions may

produce atomic hydrogen, which can diffuse into the metal and embrittle it. In corrosive environments[153], these precipitate-rich boundaries become anodic and preferentially corrode[93]. Pits act as stress concentrators and crack initiation sites, leading to localized material removal[151].This weakens the alloy and reduces its load-bearing capability, thereby lowering both strength and hardness. This undermines the grain boundary strength, leading to grain boundary decohesion and embrittlement. This reduces ductility, making the alloy more susceptible to crack propagation under stress. Conditional fracture toughness value of all five conditions sample is decreasing because of formation of pits and its maximum in case of SHT+PA+90% CR sample due to dislocation and grain boundary strengthening[20,21].

5.6.3 Influence of precipitation on corrosion behaviour

In SHT sample supersaturated solid solution is formed. Electrochemical heterogeneity is low, less galvanic coupling[154]. However, presence of Cu-rich particles and residual intermetallic can still initiate localized pitting[39] as shown in Fig.5.16(a). Corrosion Rate is generally lower (potential difference between secondary phase particles and matrix is smaller) than peak-aged due to no precipitates (potential difference between precipitates and matrix is very high)[155,156]. In SHT+PA sample precipitation of Mg_2Z_3 (η") occurs in the matrix and at grain boundaries. Grain Boundary Precipitates (GBPs) + precipitate-free zones (PFZs) form micro-galvanic cells[157] . η"-phase is anodic to the matrix promotes intergranular and pitting corrosion[2]. Electrochemical heterogeneity is higher due to strong cathodic precipitates[60,158]. Therefore large no. of pits of big size is perceived on the sample surface (Fig.5.16(b)). In the SHT +45% CR sample, no precipitates are observed in the matrix or along the grain

boundaries[159]. The cold rolling process introduces dislocations and forms sub-grains, which contribute to improved corrosion resistance[160]. That is why very small size pit in very small no. is spotted in SHT +45% CR sample (Fig. 5.16(c)). In the SHT+60% WR sample, coarse precipitates are formed, which increase galvanic coupling between the precipitates and the matrix. However, warm rolling also leads to grain refinement, which improves corrosion resistance and making it better than that of the SHT+PA sample[161]. Thus, moderate size corrosion pit in moderate no. is observed in SHT+60% WR sample (Fig.5.16(d)). In SHT+PA+90% CR sample, during cold rolling, the mechanical deformation breaks up coarse, continuous precipitates (especially at grain boundaries) and redistributes them more finely and uniformly throughout the matrix[162]. These smaller precipitates are often less electrochemically active compared to large ones[163]. This reduces galvanic coupling between precipitates (which act as cathodes) and the aluminum matrix (which acts as anode), decreasing localized corrosion such as pitting and intergranular attack[64]. Cold rolling increases dislocation density, which enhances diffusion paths and promotes quicker formation of a protective oxide layer ($Al_2\ O_3$) on the surface[164]. smaller precipitates are less likely to serve as initiation sites for pitting corrosion compared to large precipitates. As pit initiation is delayed or reduced, overall corrosion rate slows down. This oxide film acts as a barrier to corrosive species like Cl^- ions in NaCl solutions[165]. Sub-grains Have lower energy than high-angle grain boundaries are less chemically active, so they are less prone to localized corrosion. The higher dislocation density at sub-grain boundaries provides sites for uniform and fine precipitate formation[166]. This reduces the risk of continuous grain boundary precipitate networks, which are major paths for corrosion attack in alloys like 7075 Al. Sub-grains

represent a more refined internal microstructure, making it harder for corrosion to propagate. Corrosion path becomes more tortuous, decreasing the corrosion rate[167]. Therefore, very small size pit in optimum no. is noticed in SHT+PA+90% Cr sample (Fig. 5.16(e))

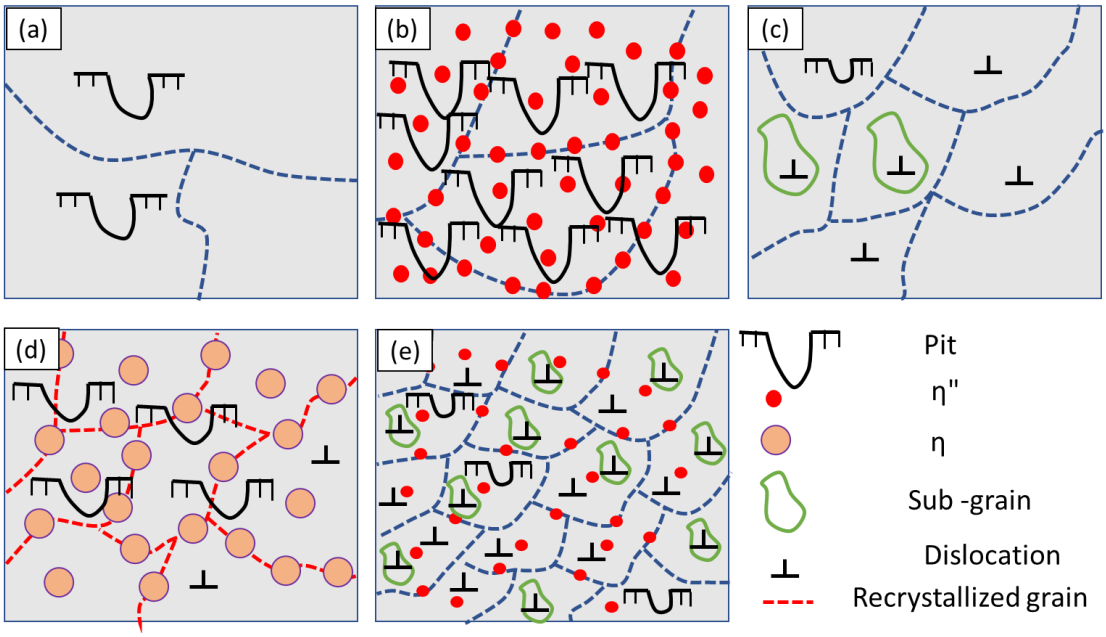

Fig.5.16 Schematic diagram illustrating the morphology of pit formation in SHT, SHT+PA, SHT+45% CR, SHT+60% WR, and SHT+PA+90% CR